Acta Biomaterialia 10 (2014) 3959–3968

Contents lists available at ScienceDirect

Acta Biomaterialia

journal homepage: www.elsevier.com/locate/actabiomat

Ultrastructural organization and micromechanical properties of shark tooth enameloid ☆

Joachim Enax [a], Anna M. Janus [b], Dierk Raabe [b], Matthias Epple [a], Helge-Otto Fabritius [b,*]

[a] Institute of Inorganic Chemistry and Center for Nanointegration Duisburg-Essen (CeNIDE), University of Duisburg-Essen, Universitaetsstr. 5-7, 45117 Essen, Germany
[b] Microstructure Physics and Alloy Design, Max-Planck-Institut für Eisenforschung GmbH, Max-Planck-Str. 1, 40237 Düsseldorf, Germany

ARTICLE INFO

Article history:
Available online 4 May 2014

Keywords:
Biomineralization
Shark tooth enameloid
Calcium phosphate
Structural hierarchy
Nanoindentation

ABSTRACT

The outer part of shark teeth is formed by the hard and mineral-rich enameloid that has excellent mechanical properties, which makes it a very interesting model system for the development of new bio-inspired dental materials. We characterized the microstructure, chemical composition and resulting local mechanical properties of the enameloid from teeth of *Isurus oxyrinchus* (shortfin mako shark) by performing an in-depth analysis using various high-resolution analytical techniques, including scanning electron microscopy, qualitative energy-dispersive X-ray spectroscopy and nanoindentation. Shark tooth enameloid reveals an intricate hierarchical arrangement of thin (50–80 nm) and long (>1 μm) crystallites of fluoroapatite with a high degree of structural anisotropy, which leads to exceptional mechanical properties. Both stiffness and hardness are surprisingly homogeneous in the shiny layer as well as in the enameloid: although both tooth phases differ in structure and composition, they show almost no orientation dependence with respect to the loading direction of the enameloid crystallites. The results were used to determine the structural hierarchy of shark teeth, which can be used as a base for establishing design criteria for synthetic bio-inspired and biomimetic dental composites.

1. Introduction

Shark teeth have different macroscopic geometries which are evolutionarily optimized for their specific biological function, i.e. the way of hunting and biting. The teeth can be classified by their geometry, e.g. as "tearing-type", "cutting-type" or "cutting-clutching type" [1–4]. The chemical and crystallographic composition of shark teeth of such different shape and function are still very similar [5]. Morphologically, the teeth of sharks consist mainly of dentin that is covered by an outer hard and highly mineralized layer in the crown area [6]. In, for example, reptiles and mammals, including humans, this outermost layer of the teeth is denoted as enamel [7,8]. In sharks, the external tooth layer has no ectodermal enamel and is, therefore, denoted as "enameloid" [9]. The enamel of mammalian teeth, including human teeth, consists of hydroxyapatite ($Ca_5(PO_4)_3OH$), associated with small amounts (~1 wt.%) of an organic matrix composed mainly of the proteins amelogenin and enamelin [10,11]. The mineral phase of shark tooth enameloid consists of fluoroapatite ($Ca_5(PO_4)_3F$) [12–15], with a fluoride content nearly as high as that of geological fluoroapatite crystals (3.1 and 3.64 wt.%, respectively) [5]. The total enameloid contains ~5–8 wt.% of organic matrix consisting of collagens and enamelins [5,16–18]. In mammalian and human tooth enamel, the hydroxyapatite forms needle-like crystallites organized in bundles ("enamel prisms") that originate at the dentin–enamel junction and are oriented perpendicular to the tooth surface [19–21]. The outermost layer ("prismless layer") of human enamel consists of parallel oriented needle-like crystallites [22]. The fluoroapatite in shark tooth enameloid is also present in the form of elongated crystallites that constitute layers with different structural organization. These layers have been classified by the structural analysis of surface etched sectional samples [23]. Three layers of the enameloid were identified and denoted as "shiny-layered enameloid (SLE)", "parallel-bundled enameloid (PBE)" and "tangled-bundled enameloid (TBE)". Since the PBE and TBE show a gradual transition, the enameloid of sharks is generally thought to be organized into two main structural building blocks: a superficial layer (shiny layer) and an inner layer consisting of crystallite bundles with changing degrees of structural organization from distal to proximal [24]. From exterior to interior, the well-organized crystallite bundles of the PBE change to a less ordered TBE. Reaching the dentin–enameloid junction, no defined bundles are visible in the TBE, but randomly arranged crystallites [24]. The formation of

☆ Part of the Biomineralization Special Issue, organized by Professor Hermann Ehrlich.

* Corresponding author. Tel.: +49 (0) 211 6792 373; fax: +49 (0) 211 6792 333.
E-mail address: h.fabritius@mpie.de (H.-O. Fabritius).

http://dx.doi.org/10.1016/j.actbio.2014.04.028
1742-7061/

shark tooth enameloid can be subdivided into three phases of development: first, the formation of the matrix; second, the mineralization of the enameloid; and finally, the maturation of the enameloid [25–27]. The individual fluoroapatite crystallites nucleate and grow in tubular vesicles formed by the odontoblasts. During the mineralization stage, the vesicles disappear and individual crystallites in different states of organization can be observed entangled between organic, presumably collagen molecules [9]. However, little is known about the structural organization of matured shark tooth enameloid at a scale smaller than the crystallite bundles and whether and how the structure and composition influence the local mechanical properties of the material.

Recently, the correlation of structure, composition and mechanical properties in biological hard tissues [28,29] has become an important field of research that aims at the development of novel biomimetic and bio-inspired materials [30,31]. The mechanical properties of shark tooth enameloid have been investigated using mainly micro- and nanoindentation techniques [5,32]. However, this has not been performed with a resolution sufficient to analyze the local mechanical properties of small building units such as individual crystallite bundles. Therefore, we have chosen the teeth of the recent shark species *Isurus oxyrinchus* (shortfin mako shark) to study the ultrastructure and elemental distribution of the enameloid using high-resolution scanning electron microscopy (SEM) and qualitative energy-dispersive X-ray spectroscopy (EDX). We have correlated these results with the local mechanical properties obtained by nanoindentation for the shiny layer and fluoroapatite crystallite bundles indented in different directions on both axial and orthogonal planes of the teeth. The results provide valuable information that can be used as inspiration for the design of bio-inspired dental materials which exploit the advantages of natural shark tooth enameloid.

2. Materials and methods

2.1. Sample preparation and analytical methods

Individual teeth of the recent shark species *I. oxyrinchus* were purchased from commercial sources that obtain their material from a commercial fishery where the teeth were extracted, cleaned and shipped to the retailers. Since the original position of the teeth in the jaw could not be reproduced, we used only specimens with shapes and sizes qualifying them as erupted mature teeth. The taxonomical determination of the shark species was verified with the help of Dr. A. Gillis, Dalhousie University, Canada. All teeth used for the experiments were stored as delivered in dry state at room temperature. We used SEM to study the microstructure, EDX to map the elemental composition and nanoindentation to determine the local mechanical properties of the enameloid and the shiny layer. The used samples were either fractured or embedded and polished in specific orientations with respect to the geometry of the tooth.

The fractured samples were prepared by creating notches at the tip and the cutting edge of two different teeth using a jeweler's saw. A sharp blade was then placed into the notches and splinters of the tooth were produced with careful hammer strokes on the back of the blade. To investigate the structure and distribution of the organic matrix within the enameloid, selected sample pieces from both teeth were superficially etched by immersion in an aqueous ethylenediaminetetraacetic acid (EDTA) solution (0.1 mol l^{-1}; Waldeck, Germany) with 2.5% glutaraldehyde (Merck, Germany) for 2 min, as described by Fabritius et al. [33]. The samples were washed in double-distilled water (1 s) followed by 100% methanol (1 s), dehydrated in an ascending series of acetone–water (30–50–70–90–100 vol.% acetone; 5 min each) and dried in a Bal-Tec CPD 030 critical point dryer. The native and etched tooth pieces were mounted with the exposed internal surface pointing upwards onto standard aluminum SEM holders and rotary-shadowed with a 4 nm thick layer of platinum in a Gatan Precision Etching Coating System (PECS 682). Subsequently, the samples were analyzed in a Zeiss Crossbeam XB1560 FIB-SEM at an acceleration voltage of 5 kV using a 30 μm aperture and an in-lens detector at small working distances. Where necessary, contrast and brightness of the SEM micrographs were adjusted using Photoshop CS2 (Adobe Inc.).

Four different teeth were prepared for EDX mapping and nanoindentation testing by cutting them with a jeweler's saw. Two teeth were axially cut and embedded in a conductive phenolic resin containing carbon fibers (Polyfast, Struers) with their sagittal planes exposed. The resin was cured using a Buehler SimpliMet 3000 heated press (150 bar, 5 min heating time, 180 °C). The other two teeth were orthogonally cut exposing the cross-section of the crown at about half the length of the tooth. These samples were embedded in a one-component UV-curable methyl methacrylate resin (CEM 4000 Lightfix, Cloeren Technology GmbH, Wegburg) that was cured in a Struers UV-Box (3 min using the bottom source only followed by 6 min with bottom and top source together). The exposed sections of all four teeth were polished using a series of abrasive papers with decreasing grit sizes (220, 400, 600, 1000, 2500 and 4000; Hermes) followed by a 3 μm diamond suspension (Struers) and final polishing with a 0.1 μm silica suspension (Buehler; Saphir 320/330 instrument, ATM).

Nanoindentation measurements were conducted with a Hysitron TriboIndenter TI 900 equipped with a top-down closed-loop scanner that maximizes the indent-positioning accuracy. We used a Berkovich indenter (Ti 39-01, tip radius 50 nm) in displacement control mode (100 nm indentation depth) and a triangular load function (10 s–10 s). The area function was determined on a fused quartz standard from Hysitron (0.7–194 nm). On the two axially polished samples, a total number of 2575 indents were set in five rectangular patterns that cover the shiny layer and outer enameloid and were distributed along the tooth margin and one pattern located in the central region of the enameloid. The spacing between the indents was 1 μm for the first and 2 μm for the second sample. On the two orthogonally polished samples, a total number of 435 indents were set in two rectangular patterns placed at the tooth margin that covered the shiny layer and the outer enameloid. The spacing between the indents was 2 μm. The reduced elastic modulus (E_{red}) and the hardness (H) were determined according to the method of Oliver and Pharr [34].

After indentation, the samples were coated with 4 nm of platinum (Gatan PECS 682) and the quality of the indents was inspected using SEM (Zeiss Crossbeam XB1560 FIB-SEM). Elemental maps with a pixel resolution of 512×400 were recorded using the built-in Apollo XL Silicon Drift Detector (EDAX) at an acceleration voltage of 10 kV, 120 μm aperture size and a dwell time of 250 μs. The post-processing of the maps, including background subtraction combined with peak deconvolution, was performed with the EDAX Genesis software package.

Subsequently, the indented areas of selected samples were subjected to superficial etching by the application of a droplet of aqueous EDTA solution (0.1 M with 2.5 wt.% glutaraldehyde) for 1.5 h, washed with distilled water and then with ethanol, recoated with 4 nm of platinum and inspected in the SEM using a backscattered electron (BSE) detector for compositional contrast. For each indent pattern, we inspected the position of every individual indentation and assigned the data point either to the shiny layer, to a certain type of crystallite bundle of the enameloid with known orientation or to areas with exposed organic matrix, respectively. Indents that were not placed on a clearly defined structure like defects in the material or on exposed organic envelopes were excluded from

the analysis. These data were used to create maps of the reduced elastic modulus (E_{red}) and the hardness (H), and to analyze (i) the averaged and the local mechanical properties of the different layers and (ii) the orientation dependence of E_{red} and H in fluoroapatite crystallite bundles indented along and perpendicular to the long axis of the crystallites. Where appropriate, the significance of differences in the average values for E_{red} and H obtained for different teeth and different indentation directions of crystallite bundles was tested by performing two-way analysis of variance (ANOVA) followed by Tukey's multiple-comparisons tests (Origin 8.6, OriginLab Corporation).

3. Results

3.1. Microstructure and elemental distribution of the shiny layer and the enameloid of I. oxyrinchus teeth

High-resolution SEM micrographs of fractured tooth samples show that the smallest repeating structural units within the enameloid of *I. oxyrinchus* teeth (Fig. 1) are elongated fluoroapatite crystallites with a roughly hexagonal cross-section. They are 50–80 nm thick, with a length generally exceeding 1 μm (Fig. 1C). The crystallites are arranged in parallel and form bundles with different dimensions and section contours (Fig. 1B–F). These bundles form the bulk of the enameloid and are arranged in intriguing patterns. Based on their orientation with respect to the geometry of the tooth crown, we distinguished three types of bundles (Fig. 1A and B). The majority are axial bundles (labeled "3" in Fig. 1), which are oriented parallel to the long axis of the tooth. They are pervaded by ribbon-shaped radial bundles (labeled "2" in Fig. 1) that originate at the dentin–enameloid junction and end within the superficial shiny layer. Distally, the axial bundles are covered by a single layer of parallel arranged circumferential bundles (labeled "1" in Fig. 1). These bundles cover the full length of the tooth crown and their section contours vary from roughly circular over elliptic to band-shaped. Individual circumferential bundles are frequently separated by radial bundles that proceed between them (Fig. 1A, E and F). The outermost layer of *I. oxyrinchus* teeth is the ~5 μm thick shiny layer that tightly covers the circumferential bundles (Fig. 1B, E and F). In native fractured samples, this layer consists of randomly oriented solid polyhedral structures that form a continuous smooth outer surface (Fig. 1B). The proximal portion of the shiny layer is regularly pervaded by the distal ends of radial crystallite bundles (Fig. 1B, E and F). In polished samples that were superficially etched using EDTA, the shiny layer appears to contain numerous randomly oriented fluoroapatite crystallites that resemble those forming the enameloid bundles in shape and size (Fig. 1E). These crystallites appear at the same contrast as those in the enameloid in backscattered electron micrographs that are sensitive to the composition of samples (Fig. 1E), whereas the material surrounding them appears at different contrast.

In fractured native samples, the clearest sign for the presence of soft organic matter within the enameloid was observed in areas where two fluoroapatite crystallite bundles were contacting each other (Fig. 2A). Here, crystallite bundles are often covered by a smooth layer that shows clear imprints from crystallites of neigh-

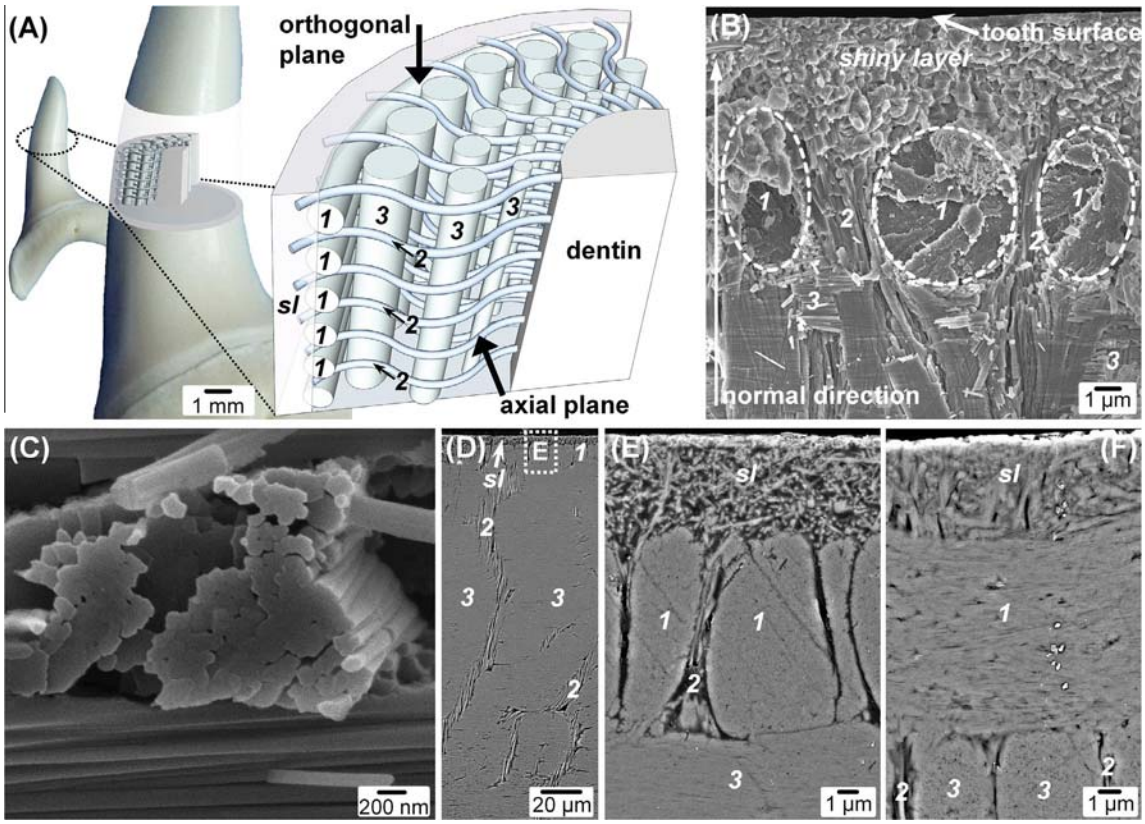

Fig. 1. Enameloid microstructure of teeth of *I. oxyrinchus*. (A) Schematic model depicting the locations of the analyzed tooth regions and the spatial arrangement of the fluoroapatite crystallite bundles in the enameloid. The shapes and trajectories of the bundles are simplified and their sizes are not in scale to each other. (B) Scanning electron micrograph showing the real arrangement of differently oriented crystallite bundles and the ultrastructure of the shiny layer on a fracture plane corresponding to the axial plane of the sketch in (A). (C) Scanning electron micrograph showing shape and size of individual fluoroapatite crystallites that form the bundles constituting the enameloid. (D) Backscattered electron micrograph of an axially polished sample etched with EDTA, showing the entire thickness of the enameloid and the structural arrangement of the crystallite bundles. (E) Detail of (D) showing the distal margin of the enameloid and the ultrastructure of the shiny layer (sl) after partial demineralization. Below the shiny layer, crystallite bundles in different orientations are visible. (F) Backscattered electron micrograph of the distal margin of the enameloid on an orthogonally polished sample corresponding to the orthogonal plane of the sketch in (A). sl: shiny layer; 1: Circumferential bundles; 2: Radial bundles; 3: Axial bundles.

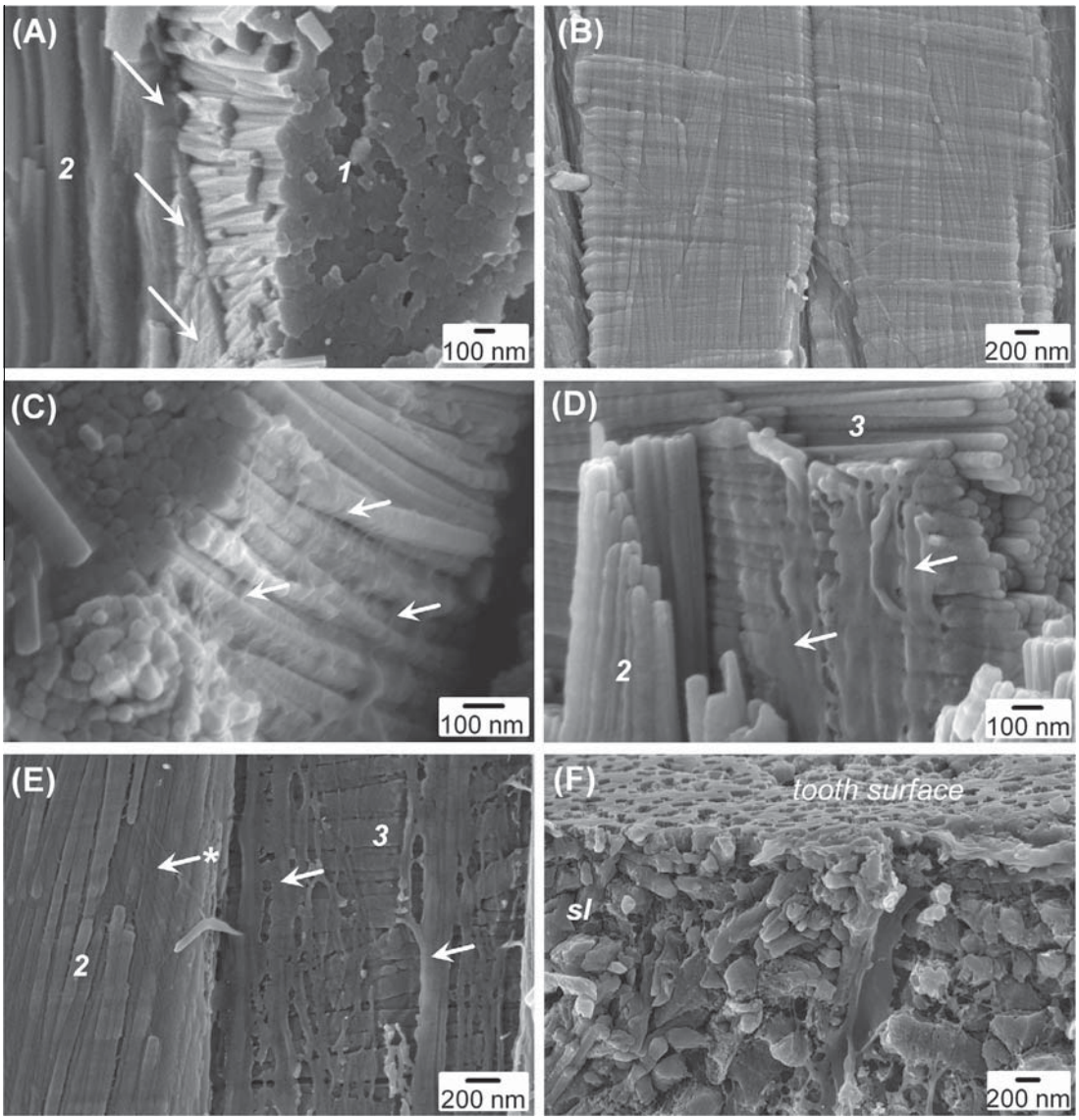

Fig. 2. Ultrastructure of the mineral phase and the organic matrix in the enameloid and the shiny layer of *I. oxyrinchus* teeth. (A) Detail of the interface between two native, differently oriented crystallite bundles, showing the organic envelope (arrows). (B–F) Scanning electron micrographs of samples which were gently etched with aqueous EDTA solutions. (B) Organic matrix layer covering a crystallite bundle with imprints of the missing neighboring bundle. (C) Detail of crystallites fragmented by partial demineralization, with attached organic filaments (arrows). (D, E) Differently oriented crystallite bundles, covered with envelopes of filamentous organic matrix (arrows). The crystallites are shown in different stages of partial demineralization. (F) Magnified image of the etched tooth surface and the underlying shiny layer, showing partially decomposed polyhedral crystallites with interspersed residual organic matrix filaments. 1: Circumferential bundles; 2: Radial bundles; 3: Axial bundles.

boring bundles that have different spatial orientations (Fig. 2B). Between individual crystallites, no traces of organic matrix were observed, neither in the native state (Figs. 1C and 2A) nor in samples that were gently etched using aqueous EDTA solutions (Fig. 2C). The superficial dissolution of fluoroapatite caused by the etching solution affects the shape of the crystallites in such a way that the hexagonal cross-section is smoothed out to a round shape. In addition, the formerly sharp fracture edges of the crystallites become rounded. A significant decrease in length is not observed (Fig. 2C and D). Etching of the enameloid reveals that each individual crystallite bundle, regardless of its orientation, has an envelope of organic material. These envelopes can be observed as frayed layers consisting of smooth parallel fibrous structures that are located between adjacent crystallite bundles (Fig. 2D and E). The smallest components observed are ~20–30 nm thick filaments adhering to crystallites located at the margins of a bundle. In most of the cases, their orientation is perpendicular to the long axes of the crystallites (Fig. 2C). Within the shiny layer, the demineralization exposes fibrillar organic matrix structures that are similar in appearance but more randomly oriented and distributed (Fig. 2F). In the surface of the shiny layer, numerous holes appear. The size of the residual solid particles forming the surface resembles that of the polyhedral structures observed in the bulk of the shiny layer (Fig. 2F).

The signals for the elements magnesium (Mg), sodium (Na), calcium (Ca), phosphorus (P) and fluorine (F) all show a homogeneous intensity over the entire thickness of the enameloid, as demonstrated by qualitative energy-dispersive X-ray spectroscopy (EDX) maps, recorded on axial sections of the teeth (Fig. 3A). Compared to the distal area of the dentin included in the map, the signal intensity in the enameloid is higher for Ca, P and F, lower for Mg and without obvious difference for Na (Fig. 3A). The second set of EDX maps was recorded close to the tooth surface at a magnification that allows us to compare the shiny layer and the distal (circumferential) crystallite bundles of the enameloid. The maps show increased signals for Na and Mg in the shiny layer, whereas

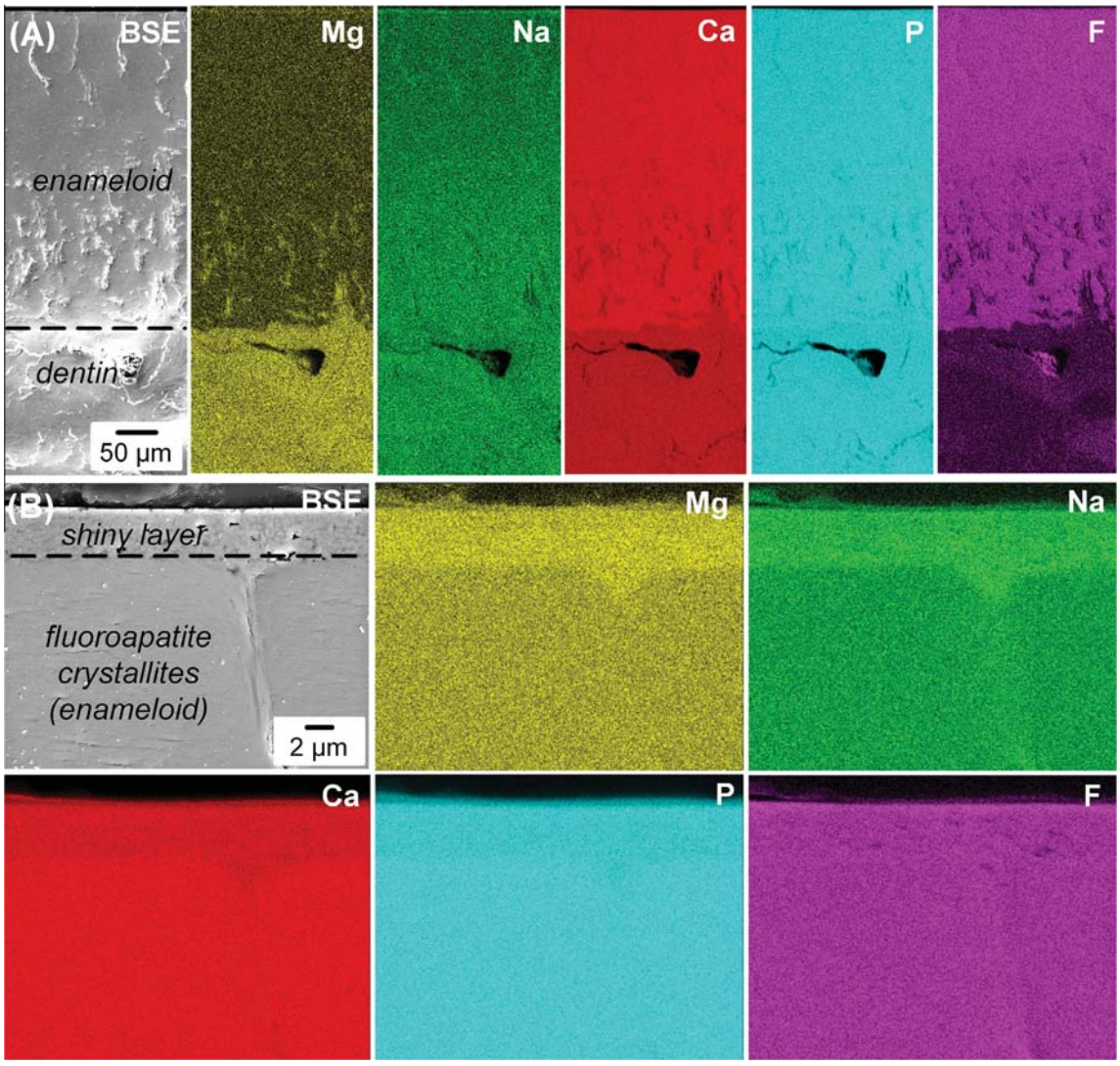

Fig. 3. Qualitative EDX mappings recorded on a polished axial section of an *I. oxyrinchus* tooth, showing the distribution of Mg, Na, Ca, P and F in the enameloid crystallites, the dentin and the shiny layer. (A) Elemental maps of the entire thickness of the enameloid, including the enameloid–dentin junction and the distal part of the dentin. (B) Elemental maps of the shiny layer and the underlying fluoroapatite crystallite bundles. The contents of Mg and Na are higher in the shiny layer than in the crystallite bundles, but slightly lower for Ca, P and F.

the signals for Ca, P and F are slightly lower than in the underlying crystallite bundles (Fig. 3B).

3.2. Local mechanical properties of the shiny layer and the enameloid of I. oxyrinchus teeth

The local mechanical properties of the shiny layer and the enameloid crystallite bundles in *I. oxyrinchus* enameloid were probed by nanoindentation on teeth that were sectioned either axially or orthogonally. Consequently, the fluoroapatite crystallites in axial and circumferential bundles were indented in two different directions: parallel to the long axis of the crystallites and perpendicular to the long axis of the crystallites (Fig. 1A and Table 1). Due to their trajectories and the tapered geometry of the tooth crown, the fluoroapatite crystallites in radial bundles were indented at a slightly tilted angle in both axially and orthogonally polished samples (Fig. 1A and Table 1). The data points obtained for each probed sample were grouped by the type of indented structure. The results show that the average reduced elastic modulus E_{red} (91 ± 12 GPa) of the shiny layer is lower and the average hardness H (5.5 ± 1.0 GPa) is higher than that of the enameloid (E_{red}: 103 ± 11 GPa; H: 4.9 ± 0.7 GPa) regardless of the probed orientation of the crystallite bundles (Table 1). The average stiffness and hardness values obtained for different indentation directions of crystallite bundles of all four probed teeth vary slightly. The highest stiffness values were measured parallel to the long axis of the fluoroapatite crystallites (E_{red}: 107 ± 9 GPa) followed by slightly lower values for perpendicular to the long axis (E_{red}: 98 ± 10 GPa). For the hardness, we observed the opposite with higher values perpendicular to the long axis (H: 5.1 ± 0.7 GPa) than parallel to the long axis (H: 4.9 ± 0.5 GPa). The lowest values for stiffness and hardness were measured oblique to the long axis of the crystallites (E_{red}: 90 ± 11 GPa; H: 4.5 ± 1.1 GPa) (Table 1). This trend persists when comparing the average values for E_{red} and H obtained for the same bundle types and indentation directions of each individual tooth sample, but the absolute values scatter somewhat (Table 1). The statistical significance of the results was tested by performing two-way ANOVA for E_{red} and H using the different tooth samples (1, 2 and 3) and the different indentation directions (parallel and perpendicular to the long axis of the crystallites) as

Table 1
Average values with standard deviation for the reduced elastic modulus E_{red} and the hardness H, obtained by nanoindentation for the enameloid crystallite bundles and the shiny layer of *I. oxyrinchus* teeth.

Layer		Average	E_{red} (GPa)	H (GPa)
Shiny layer (total)			91 ± 12	5.5 ± 1.0
Enameloid (total)			103 ± 11	4.9 ± 0.7
Fluoroapatite crystallites		Loading direction		
		Parallel to long axis	107 ± 9	4.9 ± 0.5
		Perpendicular to long axis	98 ± 10	5.1 ± 0.7
		Oblique to long axis	90 ± 11	4.5 ± 1.1
Tooth no., exposed plane	Crystallite bundle type	Loading direction		
1, axial*	Circumferential	Parallel to long axis	110 ± 6**	5.0 ± 0.3
	Axial	Perpendicular to long axis	100 ± 8**	5.3 ± 0.5
	Radial	Oblique to long axis	96 ± 7	5.1 ± 0.8
2, axial	Circumferential	Parallel to long axis	95 ± 9	5.2 ± 0.7
	Axial	Perpendicular to long axis	n.a.	n.a.
	Radial	Oblique to long axis	89 ± 9	4.2 ± 1.1
3, orthogonal*	Axial	Parallel to long axis	105 ± 5**	4.2 ± 0.2
	Circumferential	Perpendicular to long axis	91 ± 7**	4.5 ± 0.5
	Radial	Oblique to long axis	86 ± 10**	4.2 ± 0.5
4, orthogonal*	Axial	Parallel to long axis	91 ± 10**	3.8 ± 0.5
	Circumferential	Perpendicular to long axis	79 ± 10**	3.5 ± 0.7
	Radial	Oblique to long axis	77 ± 13	3.1 ± 0.8

The results are sorted by layer, loading direction of the fluoroapatite crystallites independent of bundle location and orientation, and by type of bundle and loading direction in the four different samples. Statistical analysis (two-way ANOVA) performed for E_{red} and H shows significant differences between the means obtained for the teeth 1, 3 and 4 (indicated by one asterisk, $\alpha = 0.05$). The differences between the means for the loading directions parallel and perpendicular to the long axis of the crystallites are only significant for E_{red}, but not for H (indicated by two asterisks, $\alpha = 0.05$). n.a.: not available.

factors followed by Tukey's multiple-comparisons tests. The main effect of different tested teeth was significant for the E_{red}, $F\ (2,\ 1842) = 500.03$, $p < 0.0001$, as was the main effect of indentation direction, $F\ (1,\ 1842) = 420.77$, $p < 0.0001$. The interaction of these two factors was significant, $F\ (2,\ 1842) = 5.03$, $p = 0.0066$. For the H, the main effect of different teeth was significant, too, $F\ (2,\ 1842) = 955.52$, $p < 0.0001$, but not the main effect of indentation direction, $F\ (1,\ 1842) = 2.84$, $p = 0.09$. The interaction between the two factors was also significant $F\ (2,\ 1842) = 26.58$, $p < 0.0001$. Since the absolute differences in E_{red} and H are relatively low, the representative color-coded modulus (Fig. 4B) and hardness (Fig. 4C) maps show a comparatively low contrast between the tested microstructural features. It has to be noted that in both maps the indents in the shiny layer appear to be more heterogeneously colored than those in the enameloid. In the E_{red} map, the areas of the circumferential bundles appear darkest (highest values) while in the H map, the shiny layer appears darker than the axial bundles. The brightest areas (lowest values) are those representing the circumferential bundles.

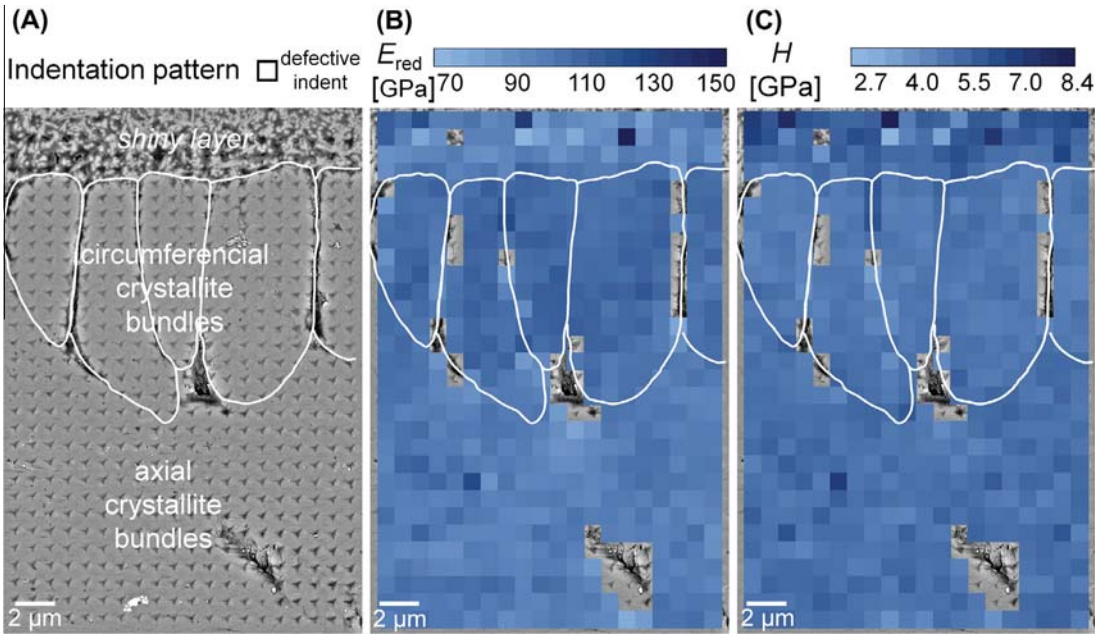

Fig. 4. Example of an indentation pattern and the resulting maps of the local mechanical properties obtained on a polished axial section of *I. oxyrinchus* enameloid, including the shiny layer and the underlying fluoroapatite crystallite bundles. (A) Indents on the sample surface, etched with EDTA to reveal the orientation of crystallite bundles. (B) Local variation of the reduced elastic modulus E_{red} and (C) the hardness H plotted on the tested polished surface.

4. Discussion

4.1. Structure of the mineral phase and the organic matrix in I. oxyrinchus enameloid

As described for other recent and fossil shark species, the enameloid of *I. oxyrinchus* teeth consists of a thin outer shiny layer and a thick layer of bundled crystallites adjacent to the dentin [24,35]. Our SEM study of untreated fractured enameloid shows that the smallest building units within the entire bundled crystallite layer are needle-like fluoroapatite crystallites with roughly hexagonal cross-sections. The shape and thickness of these crystallites correspond well to those described by Sasagawa [9] in a study by transmission electron microscopy on the development and mineralization patterns of shark tooth enameloid. In native enameloid, we observed that the crystallites are longer than those occurring in the mineralization stage of enameloid maturation [9]. However, circumferential constrictions at intervals of 300 to 500 nm appear on the long crystallites in samples that were etched using gentle demineralization protocols [33] on both fractured and axially cut and polished tooth samples. This indicates an inhomogeneous stabilization of the mineral in certain areas of the crystallites. The corresponding lengths of the etched fragments and the crystallites observed during the mineralization stage [9] suggest that the mature crystallites originate from the fusion of the smaller ones. Most probably, this occurs during the enameloid maturation when the crystallites get oriented and combined to form bundles. The dimensions of mature untreated crystallites (50–80 nm thick and >1 μm long) are comparable to those occurring in human enamel [20,36]. Within the same bundle, the crystallites are always densely packed with their long axes oriented parallel, and empty spaces or defects are rarely observed. Based on our structural analysis, the "parallel-bundled enameloid" (PBE) and "tangled-bundled enameloid" (TBE) [24,35] in *I. oxyrinchus* teeth consist mainly of axial crystallite bundles that are oriented parallel to the long axis of the tooth and pervaded by numerous ribbon-shaped radial bundles that proceed perpendicular to the long axis of the tooth (Fig. 1). The size of the radial bundles appears to decrease from their initiation sites at the dentin–enameloid junction towards the distal layers of the enameloid (Fig. 1D), where they proceed between the circumferential bundles and project into the superficial shiny layer (Fig. 1E and F). The circumferential bundles are arranged in parallel and form a terminal layer that covers the entire functional part of the tooth (Fig. 1A and B). The exact function of this layer is not yet clear, but it is safe to assume that it plays a role in the stability and fracture resistance of the thin and pointy teeth of *I. oxyrinchus*. Thus, the enameloid microstructure of *I. oxyrinchus* differs significantly from the enamel microstructure of human teeth where the crystallite bundles ("enamel prisms") are all oriented perpendicularly from the dentin–enamel junction towards the tooth surface [19–21].

The shiny layer is formed in the last stage of enameloid development [9,37]. Within the shiny layer, the demineralization exposed crystallites resembling those occurring in the bundles forming the enameloid (Fig. 1E). This indicates that the polyhedral structures observed in untreated samples (Fig. 1B) originate from subsequent growth of shorter, randomly oriented fluoroapatite crystallites that were formed as outermost layers during tooth maturation. The tooth surface is formed by a ~500 nm thick layer where these crystallites appear to be very densely packed and oriented with their long axes parallel to the surface (Fig. 1E).

The organic matrix of shark tooth enameloid has been shown to consist mainly of collagens and enamelins and its composition varies in different states of tooth maturation [16–18]. Earlier work has shown that the enameloid of *I. oxyrinchus* contains up to 5% of organic matrix [5]. However, the constituting protein types and their quantitative distribution have not been described yet. With the array of techniques that we have employed, the study of the distribution and architecture of the organic matrix implies that the fluoroapatite crystallites themselves are devoid of organic components. Instead, we observed that each individual crystallite bundle has an envelope of organic matrix with a smooth and sometimes fibrous appearance (Fig. 2A–E). In general, smaller filaments can be observed on individual crystallites at the borders of bundles that appear to connect them (Fig. 2C). In between individual bundles, the organic layers consist of coarser filaments (Fig. 2B, D and E). The layers are sufficiently thick to leave distinct imprints of the adjacent crystallite bundle when fractured (Fig. 2B). Around human enamel crystallite bundles an organic matrix with a width of ~800–1000 nm is also present [38]. Within the etched shiny layer, the demineralization exposed filamentous organic matrix structures (Fig. 2F) similar to those occurring on crystallites located at the margins of bundles in the enameloid (Fig. 2C).

The mineral of shark tooth enameloid is fluoroapatite [5,12–14]. Elemental mapping performed using qualitative EDX on an axially polished surface covering the entire thickness of the enameloid, including the enameloid–dentin junction (Fig. 3A), shows that the distribution of Mg, Na, Ca, P and F is homogeneous within the enameloid. This indicates that the entire enameloid consists of the same mineral phase. However, EDX maps recorded at higher resolution (Fig. 3B) show higher signals for Na and Mg in the shiny layer compared to the underlying crystallite bundles. In addition, the signals for Ca, P and F in the shiny layer are slightly lower. Assuming that the larger polyhedral crystallites of the shiny layer originate from similar fluoroapatite crystallites as those found in the enameloid, the EDX results suggest that the additional mineral phase of the solid polyhedral structures has a slightly different chemical composition. Both Mg and Na can occur as substituents for Ca within the fluoroapatite lattice. Mg as a substituent is known to reduce the crystallinity of apatite, while Na has no effect on the crystallinity [11]. At present, it is not known whether the compositional differences are already present during the formation and maturation of the shiny layer or if they could also be the result of superficial remineralization processes occurring during the lifetime of the tooth when it is exposed to seawater.

4.2. Micromechanical properties of the shiny layer and enameloid of I. oxyrinchus teeth

The local mechanical properties of the shiny layer and of the differently oriented crystallite bundles in *I. oxyrinchus* enameloid were probed by nanoindentation on sectioned teeth that were subsequently polished to minimize the surface roughness (Fig. 4). In contrast to microindentation (e.g. Vickers hardness test), nanoindentation allows us to map the local mechanical properties of biological materials with high resolution, thus enabling us to determine possible mechanical anisotropy caused by structural and compositional differences on the enameloid crystallite level (see, e.g. Ref. [39] and Table 1). In addition, we obtained global information on stiffness (E_{red}) and hardness (H) of the enameloid (E_{red}: 103 ± 11 GPa; H: 4.9 ± 0.7 GPa) and the shiny layer (E_{red}: 91 ± 12 GPa; H: 5.5 ± 1.0 GPa), respectively (Table 1). The values for enameloid correspond quite well to those presented by Enax et al. [5] for the same species and the small differences can most probably be attributed to biological variability and the different experimental protocol used in that study. Compared to other shark species such as *Galeocerdo cuvier* [5], *Carcharias taurus* [32] and *Sphyrna tiburo* [32] the enameloid of *I. oxyrinchus* has a higher stiffness and hardness. These deviations in the values may partly be caused by inherent methodological reasons brought about by dif-

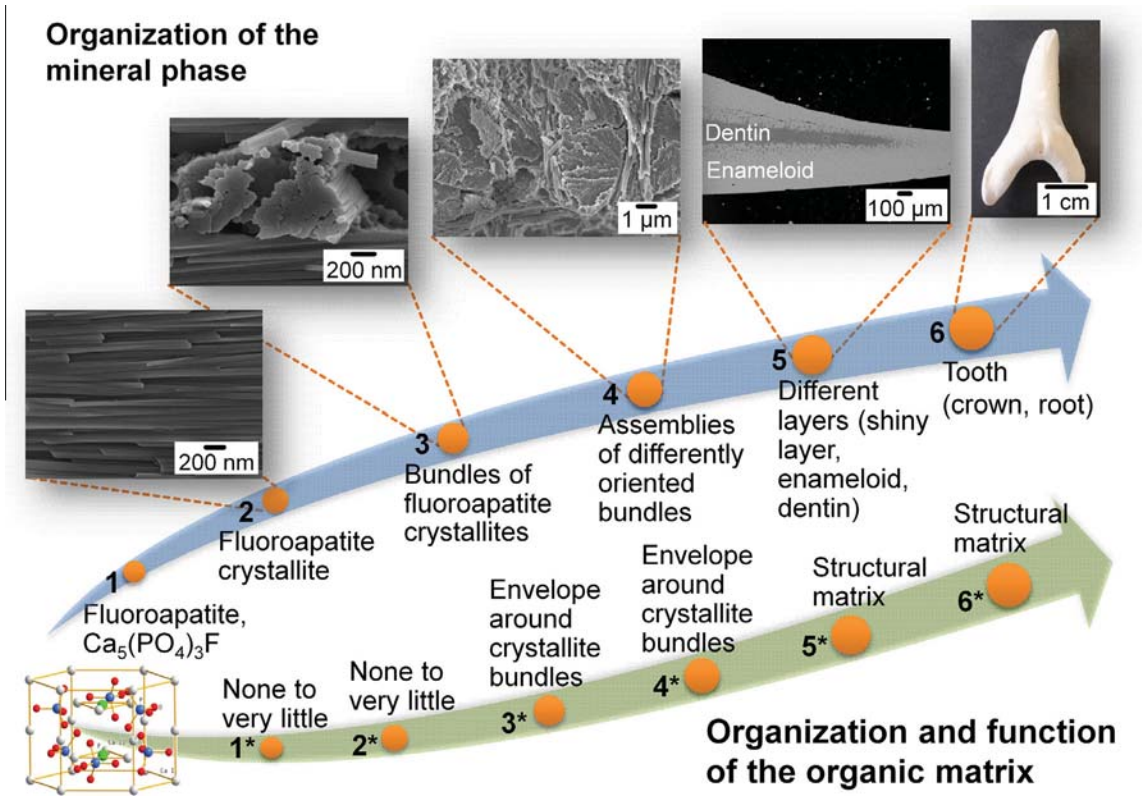

Fig. 5. Structural hierarchy of shark teeth as derived from teeth of *I. oxyrinchus*, based on the inorganic (mineral) phase (top) and on the organic matrix (bottom). The inserts show scanning electron micrographs of teeth of *I. oxyrinchus* at the corresponding length scales.

ferent experimental setups and sample preparation methods. However, it is more probable that the mechanical properties vary because of differences in structure and composition of the mineral crystallites and the organic matrix forming the enameloid, both of which are the result of evolutionary adaptations for different functions of the teeth in different species [1–4].

The average values for stiffness (E_{red}) and hardness (H) obtained for the two main indentation directions parallel (E_{red}: 107 ± 9 GPa, H: 4.9 ± 0.5 GPa) and perpendicular (E_{red}: 98 ± 10 GPa, H: 5.1 ± 0.7 GPa) to the long axes of the fluoroapatite crystallites differ only slightly (Table 1), which is in agreement with the very low elastic anisotropy measured for fluoroapatite single crystals [40]. Statistical analysis showed that the small difference observed between different indentation directions of crystallite bundles is significant at least for the E_{red} (Table 1), indicating that the fluoroapatite crystallites are stiffer along their long axes than perpendicular to it. This would mean that there is a small degree of mechanical anisotropy in the enameloid on the level of crystallite bundles. However, the average values for E_{red} and H obtained for the same bundle type and indentation direction in the four analyzed teeth scatter and statistical analysis shows that these differences are significant as well (Table 1). This has to be attributed to the inherent intraspecific variability of the material in this biological system caused by environmental conditions, age and health status of the animals [41]. While we are not able to explain the reasons for the variations due to the lack of data on provenience and the physiological state of the animals the sampled teeth originate from, it has to be noted that the trends for E_{red} and H are the same for all tested teeth. In addition, the samples were stored and tested in a dehydrated state, and embedded in different media due to technical reasons. Thus, it is likely that our results do not exactly reflect the actual micromechanical properties of enameloid in teeth that are still in function in vivo. Due to embrittlement caused by the loss of water, stiffness and hardness of enameloid in its natural state can be expected to be somewhat lower than the absolute values we present for dry enameloid. However, the orientation-dependent gradients observed in dry material are unlikely to differ significantly from hydrated material, especially since the enameloid contains only ~5 wt.% of organic material [5]. Taking these factors into account, the observed differences in E_{red} and H along and across the long axis of the bundled fluoroapatite crystallites may also be a chance finding. Thus, we have to conclude that the fluoroapatite crystallites are essentially mechanically isotropic. This is remarkable since in many other biological mineralized fiber-based composites, the mechanical properties are increasingly anisotropic when the tested building blocks become smaller because the inherent properties of single, mostly anisotropic constituents gain importance [39,42–44]. Although our data provide evidence for a strong structural anisotropy in the enameloid of *I. oxyrinchus*, this is not reflected in the local mechanical properties. This implies that the structural organization of the fluoroapatite crystallite bundles within the enameloid does not play a prominent role in the overall mechanical stability of the tooth crown. However, it may very well be that the different orientations of the crystallite bundles are important for damage resistance, since their structure and arrangement are ideally suited for guidance and deflection of cracks and thus energy dissipation.

Although both structural organization (Figs. 1 and 2) and composition (Fig. 3) of the shiny layer differ from the crystallite bundles of the enameloid, their stiffness and hardness are comparable (enameloid: E_{red}: 103 ± 11 GPa, H: 4.9 ± 0.7 GPa; shiny layer: E_{red}: 91 ± 12 GPa, H: 5.5 ± 1.0 GPa; Table 1). Our structural and compositional data show no indication that the level of mineralization of both layers differs greatly. The stiffness of the enameloid is slightly higher than that of the shiny layer, which is probably brought about by the much denser packing of the needle-shaped crystallites. However, the hardness of the enameloid is slightly lower than that of the shiny layer. Since the differences

in the values are small, it is difficult to assess reasons for the deviations in hardness between the two layers at the current state of the analysis. This could be clarified by in-depth studies of the plastic deformation and damage mechanisms at small length scale in both the enameloid and the shiny layer.

4.3. The structural hierarchy of shark teeth using the teeth of *I. oxyrinchus* as a model

From a materials science point of view, biological hard tissues such as shark teeth are composite materials consisting of small organic and inorganic constituents that are combined with increasing structural complexity on different length scales (e.g. Ref. [29]). Their often exceptional physical properties are ideally adapted to the function of the material and frequently the result of smart variations of structure and composition and a hierarchical organization (e.g. Refs. [30,31,45]). Understanding the correlations of structure, composition and properties of a biological material is crucial if it is intended to be used as a model to design e.g. novel bio-inspired materials [42,43,46]. Therefore, based on previous work [5] and our detailed structural analysis, we determined the structural hierarchy of shark teeth using *I. oxyrinchus* as model organism. Based on the mineral phase, it is possible to define six hierarchical levels (Fig. 5, levels 1–6). The organization of the organic matrix follows the structural hierarchy of the mineral phase (Fig. 5, levels 1∗–6∗). The (formally) smallest structural unit of *I. oxyrinchus* teeth is the hexagonal fluoroapatite unit cell $Ca_5(PO_4)_3F$ (1). $Ca_5(PO_4)_3F$ forms hexagonal, 50–80 nm thick and >1 μm long fluoroapatite crystallites (2). The crystallites are arranged into tightly packed bundles (3), each having an envelope of organic matrix (3∗). Differently oriented bundles form assemblies (4) found in the three different layers: shiny layer, enameloid and dentin (5), which form the whole macroscopic tooth with crown and root (6).

Based on this model, it is conceivable to draw inspiration for synthetic materials for specific applications from single hierarchical levels. Considering the requirements that dental restoration materials have to fulfill, both the composition and the structural organization of *I. oxyrinchus* teeth on the lower hierarchical levels (up to level 3) would have advantages compared to synthetic dental materials that are commercially available, like ceramics (e.g. based on aluminum oxide or zirconium dioxide), polymers (usually based on polymethylmethacrylate, PMMA), amalgam and gold [47]. For instance, these artificial materials lack the continuous remineralization by precipitation of calcium phosphate from saliva [48], and the combination of high load resistance and fracture toughness provided by the elaborate tooth microstructure [49–51]. The most notable disadvantage of high-performance ceramics and polymers is the considerable difference of their mechanical properties compared to the native tooth enamel. These tooth restoration materials are either much harder (ceramics) or softer (polymers) than the tooth enamel in their direct contact. This leads to medium term and long term problems like failure at the interfaces and inhomogeneous abrasion of either the restored tooth surface itself or the tooth on the opposite side [47]. Such effects would be minimized by a dental material based on fluoroapatite, since its mechanical properties are similar to those of hydroxyapatite [5]. Furthermore, fluoroapatite has a higher acid resistance [52] than the hydroxyapatite of human teeth and various crystal morphologies are known [53,54]. This opens opportunities to tailor synthetic crystallites which can be used to synthesize composites with e.g. PMMA as matrix material. Finally, the mechanical isotropy of fluoroapatite crystallites observed in the enameloid of *I. oxyrinchus* implies that there is no need for elaborate arrangement of synthetic crystallites in fluoroapatite/polymer composites beyond achievement of their densest possible packing. Consequently, bio-inspired and biomimetic materials that use natural design principles and thus recreate the properties of natural teeth offer great potential to improve the performance and durability of dental materials.

5. Conclusions

To elucidate the potential of shark tooth enameloid as a model material for the development of synthetic bio-inspired dental materials, we performed a detailed structural and compositional analysis of enameloid and shiny layer from teeth of the shortfin mako shark, *I. oxyrinchus*, using high-resolution SEM and EDX. The results show that both layers have a pronounced structural anisotropy. The enameloid consists of thin and long fluoroapatite crystallites that form bundles with different dimensions which are arranged in intriguing patterns, each having an envelope consisting of organic matrix. Based on their orientation with respect to the geometry of the tooth, we distinguished different types of bundles: axial bundles oriented parallel to the long axis of the tooth, ribbon-shaped radial bundles proceeding perpendicular to the long axis of the tooth and circumferential bundles that form a terminal enameloid layer adjacent to the shiny layer. These findings were used to define the structural hierarchy of shark teeth from the nanoscopic to the macroscopic length scale. Mapping of the local mechanical properties of differently oriented crystallite bundles by nanoindentation showed that both stiffness (E_{red}) and hardness (H) are essentially isotropic with respect to the loading direction (parallel or perpendicular to the long axis of the bundled crystallites). In addition, E_{red} and H of the shiny layer and the enameloid are comparable, despite differences in structure and elemental composition. Together, these data provide a sound base for the establishment of design criteria for potential synthetic tooth restoration materials inspired by the natural design principles uncovered in shark tooth enameloid.

Acknowledgements

We thank Dr. Andrew Gillis, Dalhousie University, Canada, for help with the taxonomic determination of the shark species, and Dr. Andreas Ziegler, University Ulm, Germany, for assistance with the statistical analysis. We are grateful to Heidi Bögershausen and Herbert Faul, Max-Planck-Institut für Eisenforschung GmbH, Düsseldorf, Germany, for help with the preparation of polished samples and the nanoindentation experiments. This work was supported by the Deutsche Forschungsgemeinschaft, Germany, within the Priority Programme 1420 "Biomimetic Materials Research: Functionality by Hierarchical Structuring of Materials".

Appendix A. Figures with essential color discrimination

Certain figures in this article, particularly Figs. 1, 3–5 are difficult to interpret in black and white. The full color images can be found in the on-line version, at http://dx.doi.org/10.1016/j.actbio.2014.04.028.

References

[1] Preuschoft H, Reif WE, Muller WH. Funktionsanpassungen in Form und Struktur an Haifischzähnen. Z Anat Entwicklungsgesch 1974;143:315–44.
[2] Powlik JJ. On the geometry and mechanics of tooth position in the white shark, *Carcharodon carcharias*. J Morphol 1995;226:277–88.
[3] Frazzetta TH. The mechanics of cutting and the form of shark teeth (Chondrichthyes, Elasmobranchii). Zoomorphology 1988;108:93–107.
[4] Whitenack LB, Motta PJ. Performance of shark teeth during puncture and draw: implications for the mechanics of cutting. Biol J Linn Soc 2010;100:271–86.
[5] Enax J, Prymak O, Raabe D, Epple M. Structure, composition, and mechanical properties of shark teeth. J Struct Biol 2012;178:290–9.
[6] Lowenstam HA, Weiner S. On biomineralization. New York: Oxford University Press; 1989.

[7] Herold RC, Graver HT, Christner P. Immunohistochemical localization of amelogenins in enameloid of lower vertebrate teeth. Science 1980;207:1357–8.
[8] Kemp NE. Organic matrices and mineral crystallites in vertebrate scales, teeth and skeletons. Am Zool 1984;24:965–76.
[9] Sasagawa I. Mineralization patterns in elasmobranch fish. Microsc Res Tech 2002;59:396–407.
[10] Teaford MF, Smith MM, Ferguson MWJ. Development, function and evolution of teeth. Cambridge: Cambridge University Press; 2000.
[11] LeGeros RZ. Apatites in biological systems. Prog Cryst Growth Charact 1981;4:1–45.
[12] Glas JE. The ultrastructure of dental enamel. VI. Crystal chemistry of shark's teeth. Odontol Rev 1962;13:315–26.
[13] LeGeros RZ, Suga S. Crystallographic nature of fluoride in enameloids of fish. Calcif Tissue Int 1980;32:169–74.
[14] Daculsi G, Kerebel LM. Ultrastructural study and comparative analysis of fluoride content of enameloid in sea-water and fresh-water sharks. Arch Oral Biol 1980;25:145–51.
[15] Dorozhkin SV, Epple M. Biological and medical significance of calcium phosphates. Angew Chem Int Ed 2002;41:3130–46.
[16] Moss ML, Jones SJ, Piez KA. Calcified ectodermal collagens of shark tooth enamel and teleost scale. Science 1964;145:940–2.
[17] Levine PT, Glimcher MJ, Seyer JM, Huddleston JI, Hein JW. Noncollagenous nature of the proteins of shark enamel. Science 1966;154:1192–4.
[18] Graham EE. Isolation of enamelinlike proteins from blue shark (*Prionace glauca*) enameloid. J Exp Zool 1985;234:185–91.
[19] Busch S, Schwarz U, Kniep R. Morphogenesis and structure of human teeth in relation to biomimetically grown fluoroapatite–gelatine composites. Chem Mater 2001;13:3260–71.
[20] Ang SF, Bortel EL, Swain MV, Klocke A, Schneider GA. Size-dependent elastic/inelastic behavior of enamel over millimeter and nanometer length scales. Biomaterials 2010;31:1955–63.
[21] Jeng YR, Lin TT, Hsu HM, Chang HJ, Shieh DB. Human enamel rod presents anisotropic nanotribological properties. J Mech Behav Biomed Mater 2011;4:515–22.
[22] Gwinnett AJ. The ultrastructure of the 'prismless' enamel of permanent teeth. Arch Oral Biol 1967;12:381–7.
[23] Cuny G, Rieppel O, Sander PM. The shark fauna from the Middle Triassic (Anisian) of North-Western Nevada. Zool J Linn Soc 2001;133:285–301.
[24] Cuny G, Risnes S. The enameloid microstructure of the teeth of synechodontiform sharks (Chondrichthyes: Neoselachii). J Vert Paleaontol 2005;3:8.
[25] Sasagawa I. Fine structure of dental epithelial cells and the enameloid during the enameloid formation stages in elasmobranch, *Heterodontus japonicus*. Anat Embryol 1999;200:477–86.
[26] Sasagawa I, Akai J. The fine structure of the enameloid matrix and initial mineralization during tooth development in the sting rays, *Dasyatis akajei* and *Urolophus aurantiacus*. J Electron Microsc 1992;41:242–52.
[27] Sasagawa I, Akai J. Ultrastructure and observations of dental epithelial cells and enameloid during enameloid mineralization and maturation stages in stingrays, *Urolophus aurantiacus*, an elasmobranch. J Electron Microsc 1999;48:455–63.
[28] Weiner S, Addadi L. Design strategies in mineralized biological materials. J Mater Chem 1997;7:689–702.
[29] Fabritius H, Sachs C, Romano P, Raabe D. Influence of structural principles on the mechanics of a biological fiber-based composite material with hierarchical organization: the exoskeleton of the lobster *Homarus americanus*. Adv Mater 2009;21:391–400.
[30] Dunlop JWC, Fratzl P. Biological composites. Annu Rev Mater Res 2010;40:1–24.
[31] Meyers MA, McKittrick J, Chen P-Y. Structural biological materials: critical mechanics–materials connections. Science 2013;339:773–9.
[32] Whitenack LB, Simkins Jr DC, Motta PJ, Hirai M, Kumar A. Young's modulus and hardness of shark tooth biomaterials. Arch Oral Biol 2010;55:203–9.
[33] Fabritius H, Walther P, Ziegler A. Architecture of the organic matrix in the sternal $CaCO_3$ deposits of *Porcellio scaber* (Crustacea, Isopoda). J Struct Biol 2005;150:190–9.
[34] Oliver WC, Pharr GM. An improved technique for determining hardness and elastic modulus using load and displacement sensing indentation experiments. J Mater Res 1992;7:1564–83.
[35] Gillis JA, Donoghue PCJ. The homology and phylogeny of chondrichthyan tooth enameloid. J Morphol 2007;268:33–49.
[36] Moss-Salentijn L, Hendricks-Klyvert M. Dental and oral tissues; an introduction. Philadelphia: Lea & Febiger; 1985. p. 236.
[37] Slavkin HC, Diekwisch T. Evolution in tooth developmental biology: of morphology and molecules. Anat Rec 1996;245:131–50.
[38] Ge J, Cui FZ, Wang XM, Feng HL. Property variations in the prism and the organic sheath within enamel by nanoindentation. Biomaterials 2005;26:3333–9.
[39] Fabritius H-O, Karsten ES, Balasundaram K, Hild S, Huemer K, Raabe D. Correlation of structure, composition and local mechanical properties in the dorsal carapace of the edible crab *Cancer pagurus*. Z Krist 2012;227:766–76.
[40] Sha MC, Li Z, Bradt RC. Single-crystal elastic-constants of fluorapatite, $Ca_5F(PO_4)_3$. J Appl Phys 1994;75:7784–7.
[41] Senawongse P, Otsuki M, Tagami J, Mjor I. Age-related changes in hardness and modulus of elasticity of dentine. Arch Oral Biol 2006;51(6):457–63.
[42] Nikolov S, Petrov M, Lymperakis L, Friák M, Sachs C, Fabritius H, et al. Revealing the design principles of high-performance biological composites using ab initio and multiscale simulations: the example of lobster cuticle. Adv Mater 2010;22:519–26.
[43] Nikolov S, Fabritius H, Petrov M, Friák M, Lymperakis L, Sachs C, et al. Robustness and optimal use of design principles of biological composites studied by ab initio-based multiscale simulations. J Mech Behav Biomed 2011;4:129–45.
[44] Weiner S, Wagner HD. The material bone: structure–mechanical function relations. Annu Rev Mater Sci 1998;28:271–98.
[45] Whitenack LB, Simkins Jr DC, Motta PJ. Biology meets engineering: the structural mechanics of fossil and extant shark teeth. J Morphol 2011;272:169–79.
[46] Chen PY, Lin AYM, Lin YS, Seki Y, Stokes AG, Peyras J, et al. Structure and mechanical properties of selected biological materials. J Mech Behav Biomed Mater 2008;1:208–26.
[47] Craig RG, Welker D, Rothaut J, Krumbholz KG, Stefan KP, Dermann K, et al., Dental materials. In: Elvers B (Editor-in-Chief), Ullmann's encyclopedia of industrial chemistry. Weinheim: Wiley-VCH; 2006.
[48] Hannig M, Hannig C. Nanomaterials in preventive dentistry. Nat Nano 2010;5:565–9.
[49] Bechtle S, Habelitz S, Klocke A, Fett T, Schneider GA. The fracture behaviour of dental enamel. Biomaterials 2010;31:375–84.
[50] Imbeni V, Kruzic JJ, Marshall GW, Marshall SJ, Ritchie RO. The dentin–enamel junction and the fracture of human teeth. Nat Mater 2005;4:229–32.
[51] Yahyazadehfar M, Bajaj D, Arola DD. Hidden contributions of the enamel rods on the fracture resistance of human teeth. Acta Biomater 2013;9:4806–14.
[52] Crommelin DJ, Higuchi WI, Fox JL, Spooner PJ, Katdare AV. Dissolution rate behavior of hydroxyapatite–fluorapatite mixtures. Caries Res 1983;17:289–96.
[53] Prymak O, Sokolova V, Peitsch T, Epple M. The crystallization of fluoroapatite dumbbells from supersaturated aqueous solution. Cryst Growth Des 2006;6:498–506.
[54] Wu Y-J, Tseng Y-H, Chan JCC. Morphology control of fluorapatite crystallites by citrate ions. Cryst Growth Des 2010;10:4240–2.